A Time-Domain Pilot Protection for AC Transmission Lines Connecting BESSs Based on Sequence Matching Index

Ping Xiong[1], Xiaoqian Zhu[1], Xing Wang[2], Lie Li[1], Yifan Zhao[1], Xiaoyang Yang[2,*]
[1]State Grid Hubei Electric Power Research Institute,
Wuhan 430072, China
[2]China University of Mining and Technology (Beijing),
Beijing 100083, China
*xiongp11@hb.sgcc.com.cn; zhuxq15@hb.sgcc.com.cn; zqt2200403090@student.cumtb.edu.cn; lil321@hb.sgcc.com.cn; zhaoyf17@hb.sgcc.com.cn; *bqt2400403009@student.cumtb.edu.cn*

***Abstract*—Battery energy storage station (BESS) possesses flexible operating states and complex fault characteristics. With the continuous increase in its installed capacity and number, the risk of maloperation of traditional relay protection significantly increases. To mitigate this risk, this paper presents a time-domain pilot protection that accommodates BESS's operating states and fault characteristics. Firstly, the issue of the traditional current differential protection (CDP) caused by the integration of BESS is analyzed. Subsequently, the fundamental principle of the Jaro distance is introduced, and the criteria for calculating the number of matching points and transpositions are redesigned accordingly. The Jaro distance is utilized to evaluate the matching degree of current sampling sequences between BESS side and grid side, thereby accurately identifying internal and external faults. Additionally, by introducing delayed operating current sequences in the process of calculating the number of matching points, the security issue caused by current transformer (CT) saturation is resolved. Finally, PSCAD/EMTDC simulations and digital-physical co-simulation (DPCS) testing validate the proposed protection's significant advantage. The results indicate that proposed protection algorithm offers gratifying performance in dependability, security and selectivity, and outperforms several emerging pilot protections.**

***Index Terms*—Battery energy storage station (BESS); Pilot protection; Sequence matching index; Jaro distance; CT saturation.**

I. INTRODUCTION

A. Motivation

During the accelerated development of modern power systems, the extensive use and development of renewable energy sources (RESs) provide crucial assurance for achieving the goals of carbon peaking and carbon neutrality [1]. However, the increasing installed capacity of RESs such as photovoltaics (PV) and wind power is beginning to reveal negative impacts on the grid. For instance, the inherent variability and randomness of RESs can deteriorate grid stability, worsen frequency quality, and increase peak-to-valley difference [2], [3]. By offering capabilities like frequency regulation, peak shaving, and valley filling, battery energy storage station (BESS) can address various problems arising from the integration of RESs into the power grid [4], [5]. Thus, globally, the installed capacity of BESS is steadily increasing year by year. However, the flexible operating states of BESS inevitably result in complex fault characteristics [6], causing traditional relay protection to suffer from reduced performance or even incorrect operation. This seriously threatens the safe operation of the power system and may even lead to large-scale blackouts. Therefore, it is necessary to research new protection methods that can adapt to the fault characteristics of BESS, thereby removing barriers to its large-scale integration.

B. Literature Review

PV and wind power, similar to BESS, are integrated into the grid via converters, and they share some similarities in their fault characteristics. Therefore, protection methods that adapt to the fault characteristics of PV or wind power can provide valuable references for this study. The authors in [7]–[9] modified the traditional current differential protection (CDP) to improve its performance, while these methods also have some drawbacks. For example, there is no phase selection function for protection in [7], the protection in [8] rejects in cases of high resistance faults, and the protection in [9] is unable to cope with three-phase faults. Time-domain pilot protection has been widely studied in recent years, which makes it a possibility to be an alternative to CDP owing to its outstanding operational performance. Some of these protection methods include dice similarity coefficient-based protection [10], improved Euclidean distance (IED)-based protection [11], fault detection index (FDI)-based protection [12], [13], and improved dynamic time warping (DTW) algorithm-based protection [14]. The protection methods proposed in [10]–[14] can accommodate the fault characteristics of RESs. However, the methods in [10] and [11] may misoperate in the presence of outliers, the methods in [12] and [13] do not fully consider the amplitude and phase

Manuscript received 22 September, 2025; accepted 19 October, 2025.
The research work is supported by the State Grid Hubei Electric Power CO, LTD. Science and Technology, Grant/Award No. 52153224001T.

differences of fault currents, causing rejection in some fault cases, and the method in [14] ignored the problem of singularity in the DTW algorithm, which leads to low efficiency. In addition, unlike RESs operating in inverter mode, BESS is capable of four-quadrant operation, enabling it to both absorb power from the grid and inject power into it. Obviously, BESS's fault characteristics are more complex, which may pose a challenge to the aforesaid protection methods.

Like BESS, voltage source converter-based high-voltage direct current (VSC-HVDC) systems can also operate in four quadrants. VSC-HVDC and BESS exhibit fault characteristics that are more comparable to each other than to those of PV or wind power systems. A comprehensive analysis of the factors affecting the magnitude and phase of fault current on AC-side of VSC-HVDC systems was provided in [15]. Also, the performance of the distance protection in this system was evaluated. However, no solutions were given. The authors in [16] introduced a fault phase selection element based on generalized amplitude ratio, adaptable to various operating states of BESS. The authors in [17] analyzed the impact of different operating states of BESS on distance protection and proposed a protection-control coordination method based on q-axis current injection. The authors in [18] introduced an accelerated distance protection for AC lines connecting VSC-HVDC systems to quickly identify internal faults. The authors in [19] analyzed the operating performance of CDP and proposed an improved CDP. The introduction of the hyperbolic tangent function significantly improves sensitivity of protection. However, it requires coordination with specific control strategies of modular multilevel converters (MMC) to achieve optimal performance. The authors in [20] proposed an adaptive CDP based on amplitude and phase compensation, where the compensation factors require real-time detection of BESS's operating state variations to function properly. In [21], an enhanced CDP, incorporating both magnitude and phase correction factors was proposed. It is suitable for AC-side faults in VSC-HVDC systems. Nevertheless, the requirement for its auxiliary criterion to identify non-ideal conditions, such as outliers, increases the complexity of the protection method. The authors in [22] and [23] put forward protection methods based on superimposed components. However, phasor estimation is essential for the methods in [19]–[23], and thus the inherent drawbacks of phasor estimation are inevitably introduced. A Minkowski distance-based time-domain pilot protection for AC lines connecting VSC-HVDC systems was proposed in [24], avoiding phasor estimation via discrete Fourier transform. However, the operating thresholds in [24] require precise setting based on detailed line parameters. To reduce dependency on line parameters, the authors in [25] proposed a novel high-sensitivity protection scheme. Meanwhile, the authors in [26] introduced a method combining Pearson correlation coefficient and Hausdorff distance to quantify similarity between one-mode currents at both line ends for fault identification. The approach in [25] requires voltage measurements from both terminals, making it vulnerable to potential transformer (PT) disconnection. Meanwhile, the method in [26] inherits the Hausdorff distance's sensitivity to outliers. Additionally, all approaches in [24]–[26] risk maloperation during current transformer (CT) saturation under severe fault conditions. The authors in [27] suggested a protection for lines connecting BESS using current trajectory coefficient (CTC), adaptable to CT saturation and CT error. Nevertheless, this approach exhibits insufficient sensitivity.

In summary, existing protection methods capable of adapting to fault characteristics on transmission lines connecting BESS still exhibit low sensitivity and inadequate operating speed. Moreover, most methods demonstrate significant security vulnerabilities, failing to mitigate maloperation risks caused by non-ideal conditions like CT saturation. Consequently, a high-sensitivity protection scheme with enhanced robustness and rapid operation speed for AC lines integrated with BESS remains imperative.

C. Contribution and Organization

This study offers the following significant contributions.

1. Jaro distance is first-ever introduced to the field of relay protection and redesigned by modifying the criteria for determining the number of matching points (MPs) and permutations. By virtue of this, the improved Jaro distance can be used to quantify the similarity of two current sampling sequences. This establishes the foundation of the protection proposed in this paper. The improved Jaro distance can effectively enhance the performance of relay protection.
2. By introducing a delay operating current into the calculation process of the number of matching points, security issues caused by current transformer (CT) saturation are resolved, thereby preventing misoperation of the protection system when an external fault occurs alongside CT saturation.
3. The introduction of sensitivity enhancement factors greatly improves the sensitivity of the proposed protection, ultimately resulting in a sequence matching index that can be used to distinguish between internal and external faults, and which functions correctly even in extreme fault conditions.
4. The proposed protection performance is verified through PSCAD/EMTDC and digital-physical co-simulation (DPCS) testing platform. The results show that the Jaro distance-based protection is adaptable to the fault characteristics of BESS and demonstrates superior robustness to non-ideal conditions. Furthermore, it is superior to some latest time-domain protection methods.

This paper is structured as follows. Section II explores how the CDP's adaptability is affected after the integration of the BESS and discusses its operational performance in detail. Section III describes the time-domain pilot protection principle based on sequence matching index, including basic principles of Jaro distance, criteria of MP, transposition calculation methodology for current sampling sequences, and criteria of MP considering CT saturation, which ultimately results in the flow of calculating Jaro similarity between two current sequences. In addition, sensitivity enhancement factors are introduced to improve sensitivity of the protection. Sections IV and V verify the performance of the proposed protection on PSCAD/EMTDC software and DPCS testing platform. Section VI summarizes the key points extracted from this article in terms of the characteristics of the proposed protection.

II. PERFORMANCE PROBLEM OF TRADITIONAL CURRENT DIFFERENTIAL PROTECTION CAUSED BY THE INTEGRATION OF BESSS

A. System Description

To ensure that the analysis results are more representative, an IEEE 39-bus test system containing BESS is constructed, as shown in Fig. 1. The system voltage is 230 kV, and the BESS capacity is 250 MW. The parameters of line 19-33 are referenced from [19]. Length of line 19-33 is 50 km.

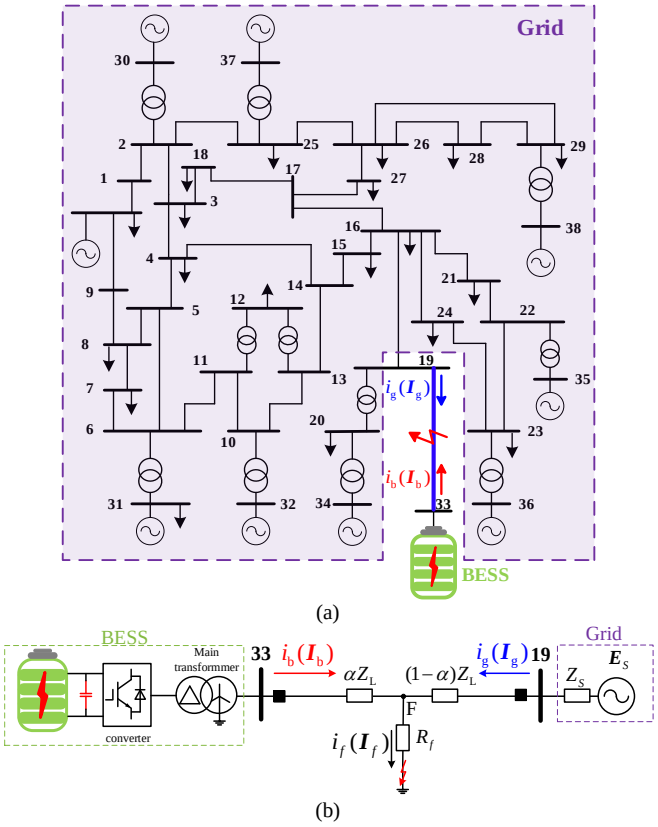

Fig. 1. IEEE 39-bus test system containing BESS: (a) Detailed model; (b) Simplified model.

B. Problem Statement

For line 33-19, the traditional CDP operating criterion can be formulated by the following equation [27]

$$\underbrace{\left|\boldsymbol{I}_{\mathrm{g}}+\boldsymbol{I}_{\mathrm{b}}\right|}_{|\boldsymbol{I}_{\mathrm{op}}|}>K\underbrace{\left|\boldsymbol{I}_{\mathrm{g}}-\boldsymbol{I}_{\mathrm{b}}\right|}_{|\boldsymbol{I}_{\mathrm{res}}|}, \tag{1}$$

where $\boldsymbol{I}_{\mathrm{op}}$, $\boldsymbol{I}_{\mathrm{res}}$ represent the operating and restraining current, $i_{\mathrm{g}}(\boldsymbol{I}_{\mathrm{g}})$ denotes the grid-side current, $i_{\mathrm{b}}(\boldsymbol{I}_{\mathrm{b}})$ denotes the BESS-side current, and K denotes the restraining coefficient, set to 0.8 in this study.

Definitions for η (amplitude ratio) and δ (phase angle difference) of two-terminal currents are as follows:

$$\eta=\frac{\left|\boldsymbol{I}_{\max}\right|}{\left|\boldsymbol{I}_{\min}\right|}=\frac{\max\left\{\left|\boldsymbol{I}_{\mathrm{g}}\right|,\left|\boldsymbol{I}_{\mathrm{b}}\right|\right\}}{\min\left\{\left|\boldsymbol{I}_{\mathrm{g}}\right|,\left|\boldsymbol{I}_{\mathrm{b}}\right|\right\}}, \tag{2}$$

$$\delta=\left|\arg(\boldsymbol{I}_{\max})-\arg(\boldsymbol{I}_{\min})\right|, \tag{3}$$

where $\boldsymbol{I}_{\max}$ and $\boldsymbol{I}_{\min}$ are defined as the larger and smaller values of $\boldsymbol{I}_{\mathrm{g}}$ and $\boldsymbol{I}_{\mathrm{b}}$. The ratio of operating current $\boldsymbol{I}_{\mathrm{op}}$ to restraining current $\boldsymbol{I}_{\mathrm{res}}$, denoted as ζ, can be defined as follows

$$\zeta=\frac{\left|\boldsymbol{I}_{\mathrm{op}}\right|}{\left|\boldsymbol{I}_{\mathrm{res}}\right|}=\frac{\left|\boldsymbol{I}_{\max}+\boldsymbol{I}_{\min}\right|}{\left|\boldsymbol{I}_{\max}-\boldsymbol{I}_{\min}\right|}=\frac{\left|\eta\mathrm{e}^{\mathrm{j}\delta}+\mathrm{e}^{\mathrm{j}0}\right|}{\left|\eta\mathrm{e}^{\mathrm{j}\delta}-\mathrm{e}^{\mathrm{j}0}\right|}=$$
$$=\frac{\sqrt{(\eta\cos\delta+1)^2+(\eta\sin\delta)^2}}{\sqrt{(\eta\cos\delta-1)^2+(\eta\sin\delta)^2}}. \tag{4}$$

From (4), the schematic diagram of CDP performance can be obtained in Fig. 2. It is known that when the phase angle difference δ becomes larger and the amplitude ratio η becomes smaller, ζ will be lower than restraining coefficient K. That is, the risk of rejection of CDP will be higher.

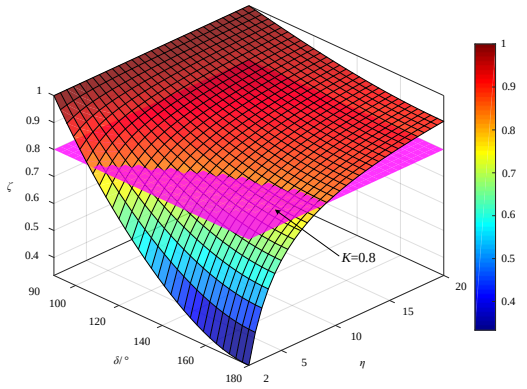

Fig. 2. Schematic diagram of CDP performance.

According to [27], the phase angle difference between grid-side and BESS-side currents is studied, showing that during the charging state (CS), an obtuse phase angle difference may occur, leading to the rejection of the CDP.

An AG fault on line 19-33, 40 km from the bus 33, with fault resistance of 60 Ω, is simulated to validate the aforementioned analysis. The BESS's capacities are set to 150 MW, 250 MW, and 350 MW. The simulation results, shown in Fig. 3, indicate that in discharging state (DCS), BESS exhibits a feed-in characteristic, with the δ between the two currents being acute. At this point, the CDP operates dependably. In contrast, when the BESS is charging, it shows a feed-out characteristic, and the δ becomes obtuse. Here, the CDP exhibits low sensitivity, and in addition, the CDP suffers from rejection as the capacity of the BESS increases. Therefore, a new protection scheme adapted to the fault characteristics of BESS is required.

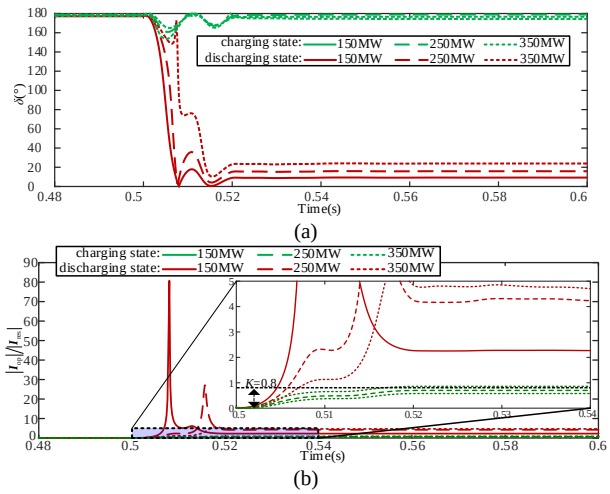

Fig. 3. δ and CDP results for different operating states and BESS capacities: (a) δ; (b) CDP results.

III. TIME-DOMAIN PILOT PROTECTION BASED ON SEQUENCE MATCHING INDEX

A. Basic Principle of Jaro Distance

The Jaro distance (JD) is an indicator of quantifying the similarity between two character sequences. Its expression is as follows [28]

$$JD=\begin{cases}0 & \text{if } m=0,\\ \frac{1}{3}\left(\frac{m}{s_1}+\frac{m}{s_2}+\frac{m-\tau}{m}\right) & \text{otherwise,}\end{cases} \tag{5}$$

where s_1 and s_2 are the lengths of two character sequences, respectively, m is the number of matching characters between the two sequences, τ is the number of transpositions among the matching characters, and the distance between two matching characters should not exceed $(\max(s_1, s_2)/2) - 1$.

Two character sequences with a length of 10 are taken as an example to illustrate the ability of Jaro distance to quantify the similarity of character sequences. In Fig. 4(a), the number of matching characters is 10, and the number of transpositions is 0. According to (5), thus, JD is 1, indicating that the sequences are completely matched. In Fig. 4(b), the number of matching characters is 8, with "J" and "K" in the same positions in both sequences, "S", "F", "G", "H", "L", and "Z" all within a distance of less than 4 in both sequences. The positions of "L" and "Z" in the two character sequences are switched, giving a transposition count of 1. According to (5), the Jaro distance is calculated as 0.825, indicating a partial match. In Fig. 4(c), there are no matching characters, and the number of transpositions is 0. According to (5), JD is 0, indicating no match between the sequences. This implies that the Jaro distance can represent the index of similarity between two character sequences. By applying the Jaro distance to relay protection, this study evaluates the similarity of currents on each side of the transmission line, thereby accurately identifying internal and external faults.

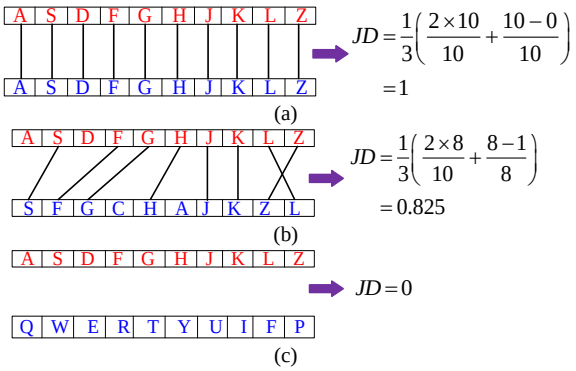

Fig. 4. Example of using Jaro distance to quantify the similarity between two character sequences: (a) Two character sequences match exactly; (b) Two character sequences match partially; (c) Two character sequences do not match at all.

B. Criteria for Matching Points Determination Applicable to Current Sampling Sequences

The traditional Jaro distance calculates the matching index between two character sequences. However, for pilot protection, the inputs are usually sampling sequences of electrical quantities, such as current sampling values. In this context, MPs cannot be determined by checking character consistency, necessitating a redesign of the criteria for MPs' determination.

Euclidean distance is used to measure the straight-line distance between two current sampling points. If the Euclidean distance between two current sampling points is sufficiently small, these points are regarded as matching.

First, the following two current sampling sequences need to be constructed:

$$\boldsymbol{A}=\{(t_1,a_1),\ldots,(t_i,a_i),\ldots,(t_n,a_n)\}, \tag{6}$$

$$\boldsymbol{B}=\{(t_1,b_1),\ldots,(t_i,b_i),\ldots,(t_n,b_n)\}, \tag{7}$$

where a_i represents the negative of the sampled value of the BESS-side current, i.e., $-i_b$, b_i represents the sampled value of the grid-side current i_g, and t_i denotes the time corresponding to the sampling point.

With a sampling frequency of 5000 Hz, the sampling period is calculated to be 0.0002 s. The analysis in this study is carried out at this sampling frequency. That is, the sampling period is much smaller than the current sampling values a_i and b_i, so the phase difference between the two current waveforms is not fully reflected by the Euclidean distance calculation. To address this issue, the sampling period Δt is stretched as follows

$$\Delta t=t_i-t_{i-1}=\frac{Range\times f_N}{f_s-f_N}, \tag{8}$$

where f_N denotes the power frequency and f_s denotes the sampling frequency. *Range* is taken from the extreme values of the two current sampling sequences $\boldsymbol{A}$ and $\boldsymbol{B}$, defined as follows:

$$\begin{cases}MAX=\max\left\{\max\limits_{i\in(1,n)}\{a_i\},\max\limits_{i\in(1,n)}\{b_i\}\right\},\\ MIN=\min\left\{\min\limits_{i\in(1,n)}\{a_i\},\min\limits_{i\in(1,n)}\{b_i\}\right\},\\ Range=MAX-MIN.\end{cases} \tag{9}$$

If the lengths of the two current sampling sequences $\boldsymbol{A}$ and $\boldsymbol{B}$ are both set to $n = f_s/f_N$, (10) becomes valid

$$t_n-t_1=(n-1)\times\Delta t=Range. \tag{10}$$

At this point, a rectangular sliding data window with both length and width equal to *Range*, as shown in Fig. 5, can be formed.

In the sliding data window illustrated in Fig. 5, the Euclidean distance between corresponding points from $\boldsymbol{A}$ and $\boldsymbol{B}$ at identical instants is given by

$$\varepsilon_i=|a_i-b_i|. \tag{11}$$

Under normal circumstances, CT error is generally within ±5 % [29]. Taking ±5 % CT error for analysis, the maximum value ε_{max} occurs at the moment corresponding to *MAX* and *MIN*, which can be obtained as

$$\varepsilon_{\max} = 0.5 \times \max\left\{\left(Range - 0.95Range\right), \left(Range - Range/1.05\right)\right\} = \\ = 0.025Range. \quad (12)$$

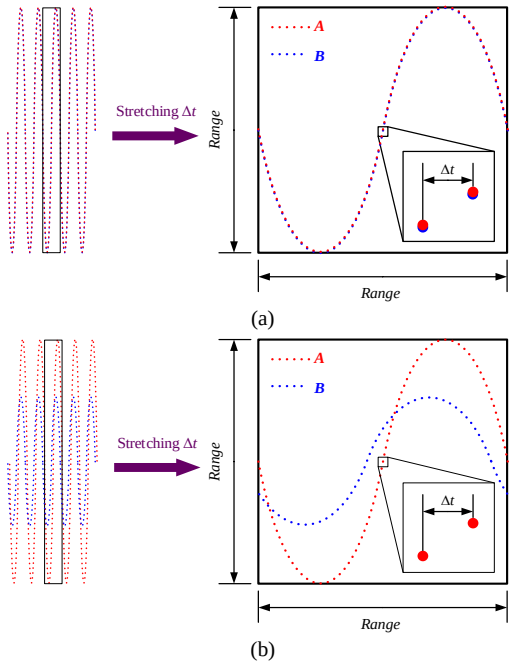

Fig. 5. Schematic of sliding data window: (a) Sliding data window during external faults or under normal conditions; (b) Sliding data window during internal faults.

Taking a certain margin into account, it is reasonable to choose 1.2 times $\varepsilon_{\max}$ as adaptive threshold μ

$$\mu = 1.2\varepsilon_{\max} = 0.03Range. \quad (13)$$

At this point, $\varepsilon_{\max}$ is smaller than μ, indicating that a_i and b_i are matched under external fault accompanied by ±5 % CT error.

Under external faults or normal conditions, as shown in Fig. 5(a), the trajectories formed by the two sequences within the data window will overlap, resulting in ε_i being much smaller than μ, and thus a_i and b_i will also be MPs. When an internal fault occurs in Fig. 5(b), the trajectories formed by the two sequences within the data window will no longer overlap, and most of the sampling points will have $\varepsilon_i > \mu$, indicating that a_i and b_i are no longer MPs.

Considering some extreme scenarios, to further enhance the resilience against CT error, it is necessary to expand the search scope. As shown in Fig. 6, when the search scope is three points on the left and right sides of the current sampling point, it is known that the minimum value of the Euclidean distance of the point furthest away from the current sampling point is $3\Delta t$, which is larger than μ. Hence, it is inappropriate to take the search scope of more than three points on both sides of the current sampling point. The search scope taken in this study is shown in Fig. 7, which evaluates two points to the left and right of the current sampling point.

In Fig. 7, the Euclidean distance $EDA(i)_{i+l}$ defined using ***A*** as the primary sequence and the Euclidean distance $EDB(i)_{i+l}$ defined using ***B*** as the primary sequence are as follows:

$$EDA(i)_{i+l} = \sqrt{(t_i - t_{i+l})^2 + (a_i - b_{i+l})^2}, \quad (14)$$

$$EDB(i)_{i+l} = \sqrt{(t_i - t_{i+l})^2 + (b_i - a_{i+l})^2}, \quad (15)$$

where l = (−2, −1, 0, 1, 2).

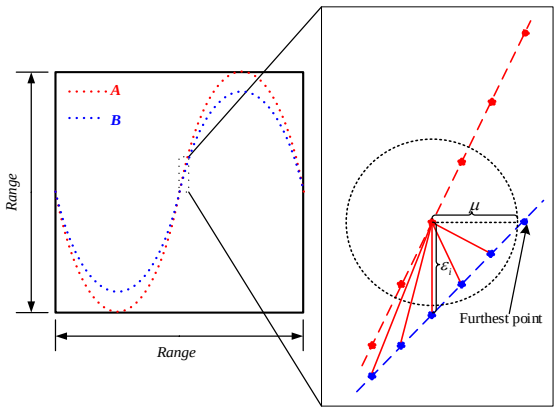

Fig. 6. Schematic of ε_i and μ under external faults accompanied by more severe CT error.

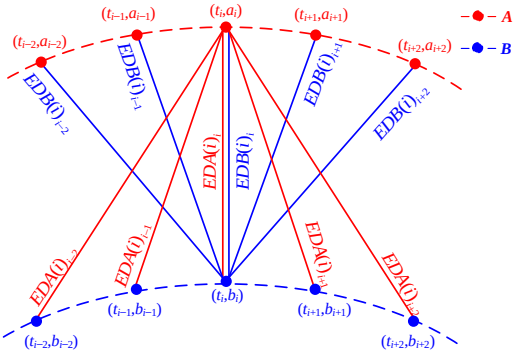

Fig. 7. Schematic of search scope.

To reduce computational burden, the search length s is set to half the length of the sliding data window, i.e., s = 0.5n. This is illustrated in Fig. 8. Within a sliding data window, the search length starts from the third point inside the window and moves to the $(s+2)^{\text{th}}$ point.

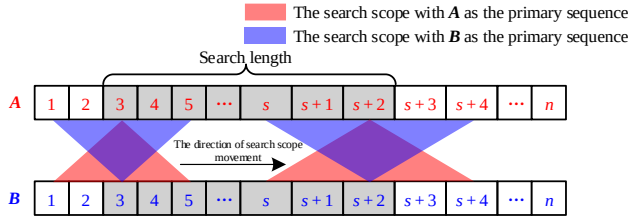

Fig. 8. Search length in the sliding data window.

The MP criteria with ***A*** as the primary sequence and with ***B*** as the primary sequence are defined, respectively, as:

$$\min_{l=(-2,-1,0,1,2)} \left\{EDA(i)_{i+l}\right\} \le \mu, \quad (16)$$

$$\min_{l=(-2,-1,0,1,2)} \left\{EDB(i)_{i+l}\right\} \le \mu. \quad (17)$$

Then, the number of MPs $m_{\boldsymbol{AB}1}$ and $m_{\boldsymbol{BA}1}$ obtained with ***A*** and ***B*** as the primary sequences are:

$$m_{\boldsymbol{AB}1} = \sum_{i=3}^{s+2} Points\ in\ \boldsymbol{A}\ that\ satisfy\ equation\ (16), \quad (18)$$

$$m_{\boldsymbol{BA}1} = \sum_{i=3}^{s+2} Points\ in\ \boldsymbol{B}\ that\ satisfy\ equation\ (17), \quad (19)$$

where $m_{\boldsymbol{AB}1}$ and $m_{\boldsymbol{BA}1}$ range from 0 to s. In a sliding data

window, the relationship between m_{AB1}, m_{BA1}, amplitude ratio η and phase angle difference δ are depicted in Fig. 9.

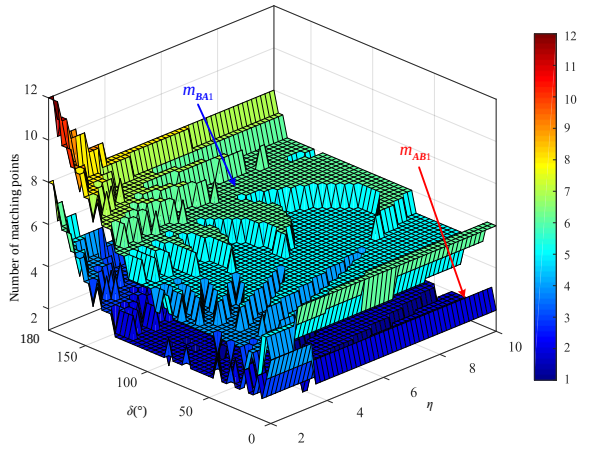

Fig. 9. The relationship between m_{AB1}, m_{BA1}, η and δ.

It is clear from Fig. 9 that there are very few MPs in most cases of internal faults. Even in the more extreme cases, i.e., small amplitude ratios and angular difference close to 180 °, the number of MPs is fewer than 13. However, in the case of external faults, there is overlap between the waveforms of ***A*** and ***B***, and the number of MPs is close to 50. In this way, the variation in the number of MPs can help distinguish between internal and external faults.

C. Criteria for Matching Points Determination Considering CT Saturation

Figure 10 presents the calculation results of m_{AB1} and m_{BA1} for an external fault with CT saturation. The waveforms of ***A*** and ***B*** will exhibit differences in the saturation zone. Consequently, the MPs calculated in a sliding data window, using the criteria from (16) to (19), will experience a decline.

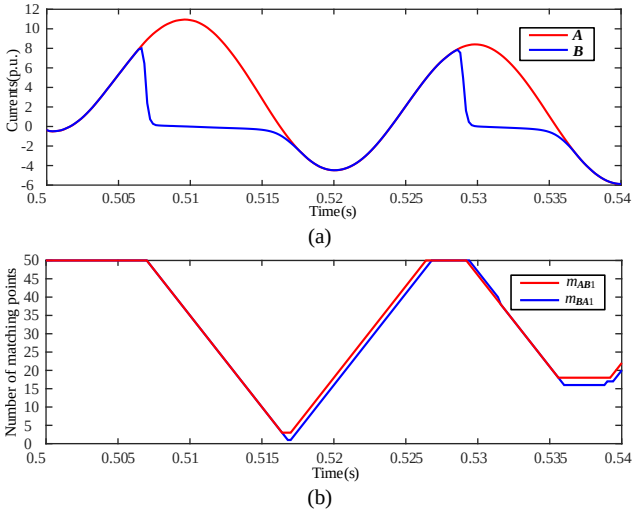

Fig. 10. Calculation results of m_{AB1} and m_{BA1}: (a) Waveforms of ***A*** and ***B***; (b) m_{AB1} and m_{BA1}.

To attenuate the detrimental effect of CT saturation on the calculation of MPs, the delayed operating current sequence ***C*** is developed by delaying the original operating current sequence by 1/2 power frequency cycle

$$\boldsymbol{C} = \{(t_1, c_1), \ldots, (t_i, c_i), \ldots, (t_n, c_n)\}, \tag{20}$$

where $c_i = b_{i-n/2} - a_{i-n/2}$.

As shown in Fig. 11, ***C*** overlaps with ***B*** in the saturation zone. Therefore, the overlap zone can be used to increase the number of MPs during CT-saturated external fault.

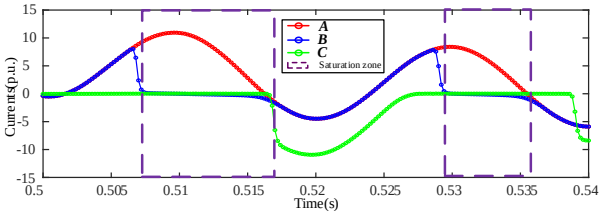

Fig. 11. Waveforms of ***A***, ***B***, and ***C***.

With the aid of cosine similarity to identify any overlapping between the sequences, the following angles are defined:

$$\theta_A(i)_{i+l} = \arccos\left[\frac{d(d+l)\Delta t^2 + c_i a_{i+l}}{\sqrt{(d^2\Delta t^2 + c_i^2)((d+l)^2\Delta t^2 + a_{i+l}^2)}}\right], \tag{21}$$

$$\theta_B(i)_{i+l} = \arccos\left[\frac{d(d+l)\Delta t^2 + c_i b_{i+l}}{\sqrt{(d^2\Delta t^2 + c_i^2)((d+l)^2\Delta t^2 + b_{i+l}^2)}}\right], \tag{22}$$

where $\theta_A(i)_{i+l}$ are the angles between the vectors formed by the points in ***A*** and the vector formed by the point in ***C***, $\theta_B(i)_{i+l}$ are the angles between the vectors formed by the points in ***B*** and the vector formed by the point in ***C***, and d denotes the number of Δt away from the origin at the currently moment sampling point. From the procedure of calculating $\theta_A(i)_{i+l}$ and $\theta_B(i)_{i+l}$ in a search scope shown in Fig. 12, all of the above vectors have origin $(t_i - \boldsymbol{d}\Delta t, 0)$, and the domain of $\theta_A(i)_{i+l}$ and $\theta_B(i)_{i+l}$ are both $[0, \pi/2]$.

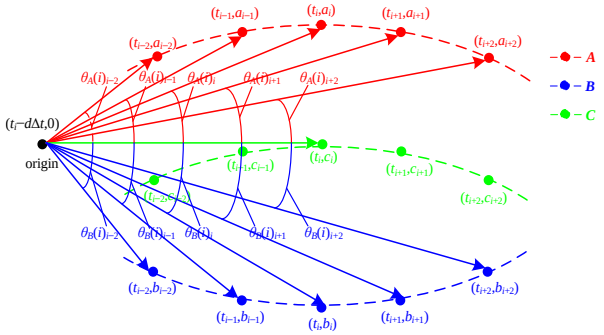

Fig. 12. Schematic diagram of the procedure for calculating θ_A and θ_B in a search scope.

Considering that the selection of the origin affects $\theta_A(i)_{i+l}$ and $\theta_B(i)_{i+l}$, to avoid making the values of $\theta_A(i)_{i+l}$ and $\theta_B(i)_{i+l}$ too large or too small, the origin is set to $(t_i - 50\Delta t, 0)$. Meanwhile, for the purpose of having fewer points to be judged as MPs in the case of internal faults and to have as many points as possible to be judged as MPs for external faults with CT saturation, under comprehensive consideration, the threshold is set as

$$\rho = 3^\circ. \tag{23}$$

For internal faults, most of the points in sequences ***A***, ***B***, and ***C*** will not be located in the overlap zone, i.e., $\theta_A(i)_{i+l}$ and $\theta_B(i)_{i+l}$ will be larger than ρ. However, for external fault with CT saturation, within saturation zone, the points in ***A*** and ***C*** or the points in ***B*** and ***C*** will be in the overlap zone, i.e., $\theta_A(i)_{i+l}$

or $\theta_B(i)_{i+l}$ will be lower than ρ. Thus, the criteria for the determination of MPs after considering CT saturation are as follows:

$$\min_{l=(-2,-1,0,1,2)}\{\theta_A(i)_{i+l}\} \le \rho, \tag{24}$$

$$\min_{l=(-2,-1,0,1,2)}\{\theta_B(i)_{i+l}\} \le \rho. \tag{25}$$

D. Criteria for Calculating the Number of Matching Points

Ultimately, after considering various fault cases, the process for calculating the number of match points m_{AB2} in a sliding data window using sequence ***A*** as the primary sequence is illustrated in Fig. 13 and explained below.

1. Start from the 3rd point in sequence ***A*** and assess whether it satisfies (16).
2. If satisfied, increment m_{AB2} by one; if not, proceed to check if it meets (24) or (25). If satisfied, increment m_{AB2} by one. If not, consider the point as non-matching.
3. Steps 1) and 2) sequentially traverse points within the search length in the sequence ***A***, ending the assessment at the $(s+2)^{th}$ point.

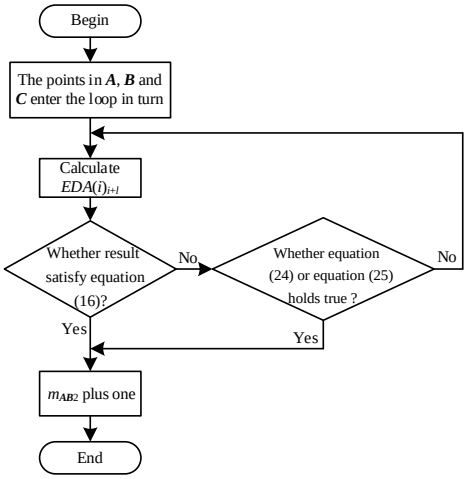

Fig. 13. Flowchart for calculating m_{AB2}.

Similarly, the process for calculating m_{BA2} within a sliding data window with sequence ***B*** as the primary sequence can be obtained by the same steps as in Fig. 13.

E. Criteria for Calculating Transpositions

In Jaro distance, the transpositions τ count the number of character transpositions among matching characters. In this study, transpositions are defined as the number of intersections in the waveforms of ***A*** and ***B***, representing the number of points where the increasing or decreasing trends differ between the waveforms of ***A*** and ***B***, as demonstrated in Fig. 14.

After the points in sequences ***A*** and ***B*** are identified as MPs, if there is a difference in the trend of increase and decrease of waveforms of ***A*** and ***B***, it is judged that transposition occurs. Define the criterion for calculating the number of transpositions as follows

$$\tau = \sum_{i=3}^{s+2} Points\ satisfy \begin{pmatrix} (a_i - a_{i-1}) \times (a_{i+1} - a_i) > 0, \\ (b_i - b_{i-1}) \times (b_{i+1} - b_i) > 0, \\ (a_{i+1} - a_{i-1}) \times (b_{i+1} - b_{i-1}) < 0 \end{pmatrix}. \tag{26}$$

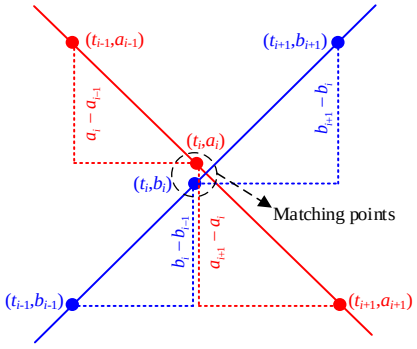

Fig. 14. Schematic diagram for intersection.

The calculation results for the number of transpositions during internal faults are presented in Fig. 15.

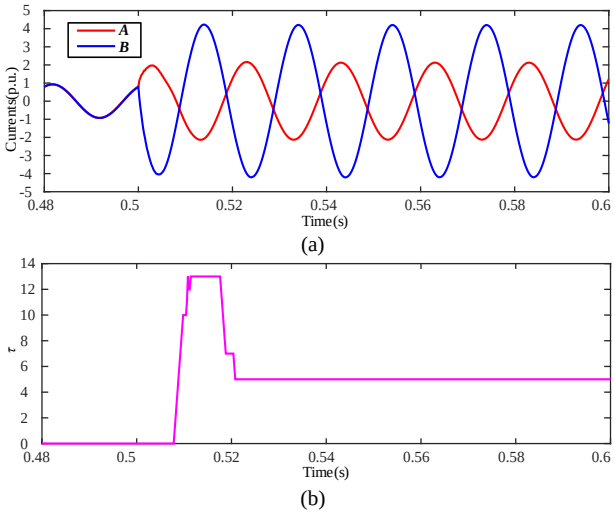

Fig. 15. Calculation results of τ during internal fault: (a) Waveforms of ***A*** and ***B***; (b) Calculation results of transpositions.

F. Sensitivity Improvement Scheme

By following the aforementioned steps to calculate m_{AB2}, m_{BA2}, and τ within a sliding data window, the Jaro similarity with ***A*** as the primary sequence (sim_{AB}) and the Jaro similarity with ***B*** as the primary sequence (sim_{BA}) can be defined as follows:

$$\begin{cases} sim_{AB} = \dfrac{1}{3}\left(\dfrac{2m_{AB2}}{s} + \dfrac{m_{AB2} - \tau}{m_{AB2}}\right), \\ sim_{BA} = \dfrac{1}{3}\left(\dfrac{2m_{BA2}}{s} + \dfrac{m_{BA2} - \tau}{m_{BA2}}\right), \end{cases} \tag{27}$$

where *sim* has a value range of 0 to 1.

To mitigate the impact of abnormal data, the calculated $\{sim_{AB}(1), \ldots, sim_{AB}(h), \ldots, sim_{AB}(s)\}$ and $\{sim_{BA}(1), \ldots, sim_{BA}(h), \ldots, sim_{BA}(s)\}$ are averaged to construct the sequence matching index (SMI)

$$SMI = 1 - \frac{\sum_{h=1}^{s} sim_{AB}(h) + \sum_{h=1}^{s} sim_{BA}(h)}{2s}. \tag{28}$$

For the purpose of observing the SMI calculation during internal and external faults, the following two fault scenarios are set up.

Fault 1 is set at 25 km of line 19-33 from the BESS-side

bus with 80-Ω fault resistance.

Fault 2 is set at bus 33, with fault resistance of 0.1 Ω, and grid-side CT is introduced with an error of +10 %.

The SMI values for Faults 1 and 2 are shown in Fig. 16. During internal faults with BESS in CS, the SMI is small and approaches that of external faults with error of CT, complicating protection threshold setting. If a low threshold is chosen, the risk of misoperation during external faults increases, reducing security of protection; if a large threshold is chosen, the sensitivity of internal fault detection may be reduced.

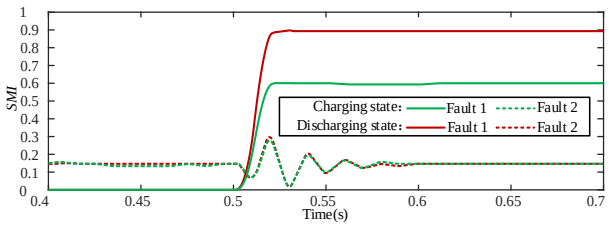

Fig. 16. SMI values during internal and external faults.

If the value of SMI is in the vicinity of 0 or 1, to improve the protection sensitivity, the SMI tends to be closer to 0 or 1. The definition of the sensitivity enhancement coefficient (SEF) ensures that when *sim* approaches 0 or 1, the SEF-transformed value converges toward 0 or 1, respectively. At this time, from (28), the sensitivity of protection is improved. Then, the expression of SEF is as follows

$$SEF = \frac{1}{1+e^{-\alpha(sim-\beta)}}, \tag{29}$$

where β is the demarcation point, taking into account the value of *sim* during external fault is close to 1, and the value of *sim* during internal fault is close to 0. This study considers a certain margin on the basis of half of the *sim* value domain and selects the demarcation point of β = 0.6; α is the scaling factor, as shown in Fig. 17. As α increases, the SEF will converge closer to 0 or 1 near the demarcation point β. If the value of α is too small, the effect of SEF will be weakened, and it will not play the role of enhancing the sensitivity. If α is too large, it will reduce the security of the protection in the presence of outliers. Taking into account the security and sensitivity of the protection, α = 20 is set.

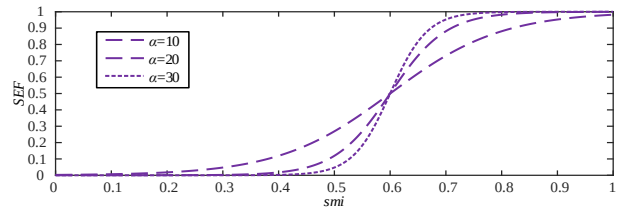

Fig. 17. Sensitivity enhancement factor.

Then, SMI can be redefined as

$$SMI = 1 - \frac{\sum_{h=1}^{s} SEF_{AB}(h) + \sum_{h=1}^{s} SEF_{BA}(h)}{2s}. \tag{30}$$

Since the value range of SMI is 0 to 1, the protection threshold (THR) is set to half its value, THR = 0.5. The protection action criterion is as follows

$$SMI > \text{THR}. \tag{31}$$

When an external fault occurs, the waveform differences between ***A*** and ***B*** are small, and SMI is less than THR, so the protection remains inactive. On the other hand, when an internal fault happens, the waveform differences between ***A*** and ***B*** are large, and SMI surpasses THR, prompting the protection to activate.

G. The Implementation of Proposed Protection

Figure 18 presents the flowchart for the protection method proposed in this study, which is detailed as follows:

1. Obtain the sequences ***A***, ***B***, and ***C***;
2. Calculate m_{AB2} and m_{BA2} by following the steps shown in Fig. 13;
3. Calculate the number of transpositions τ if the points in the sequences ***A*** and ***B*** are judged to be matched;
4. Calculate SMI by (30);
5. When the SMI surpasses THR, it is interpreted as internal fault and a trip signal is activated. If SMI is below THR, it is considered an external fault or normal condition, and no trip signal is sent.

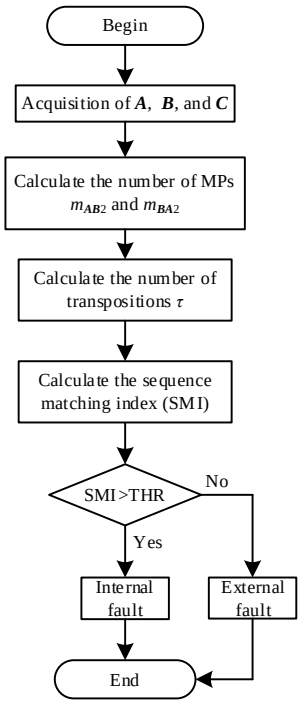

Fig. 18. Flowchart of proposed protection scheme.

IV. PERFORMANCE VALIDATION THROUGH PSCAD

This section employs electromagnetic transient simulations to quantitatively assess the protection performance under diverse fault scenarios. The system in Fig. 1(a) is developed using PSCAD/EMTDC. Various fault scenarios are introduced to test the performance of the protection. The fault inception time is set at 0.5 s.

A. The Impact of Different Fault Resistances and Fault Types

This analysis aims to evaluate the ability of SMI-based protection to handle various fault resistances and types. The fault position is positioned at midpoint (50 %) of line 19-33.

The simulation results are summarized in Table I, with the blue-highlighted part further illustrated in Fig. 19.

Table I and Fig. 19 reveal that the SMIs of the fault phases consistently surpass THR under different fault resistances and types, while the SMIs for the non-fault phases are consistently lower than THR. This suggests that the proposed protection method naturally performs phase selection. Moreover, Table I shows that the minimum sensitivity is 1.88, and the average operating time is 12.7 ms, confirming the high sensitivity and rapidity of the method in dealing with various operating states of BESS and different fault scenarios.

TABLE I. SIMULATION RESULTS AT DIFFERENT FAULT RESISTANCES AND FAULT TYPES.

Operating States	Fault Types	Fault Resistance (Ω)	*SMI*			Operating Time (ms)
			A	B	C	
Discharging State	AG	0.1	1.0	0	0	11.8
		50	1.0	0	0	12.0
		100	1.0	0	0	12.0
	ABG	0.1	1.0	1.0	0	11.8
		50	1.0	1.0	0	11.4
		100	1.0	1.0	0	11.4
	AB	0.1	1.0	0.99	0	12.0
		25	1.0	1.0	0	11.4
		50	1.0	1.0	0	11.4
	ABC	0.1	1.0	1.0	1.0	20.4
		25	1.0	1.0	1.0	11.4
		50	1.0	1.0	1.0	11.4
Charging State	AG	0.1	1.0	0	0	14.0
		50	0.98	0	0	13.8
		100	0.98	0	0	13.4
	ABG	0.1	1.0	1.0	0	13.4
		50	0.98	0.98	0	11.6
		100	0.97	0.97	0	11.8
	AB	0.1	0.94	1.0	0	12.0
		25	0.98	0.98	0	12.2
		50	0.98	0.98	0	12.2
	ABC	0.1	0.95	1.0	1.0	19.0
		25	0.97	0.98	0.98	11.8
		50	0.98	0.98	0.98	11.8

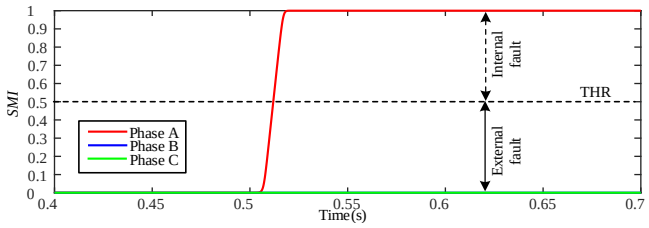

(a)

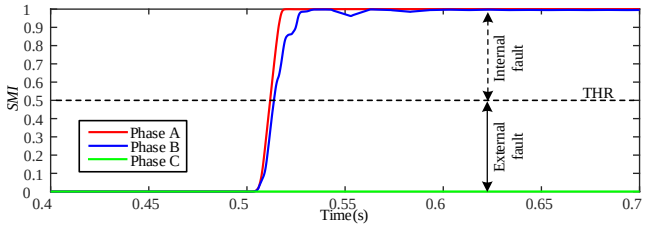

(b)

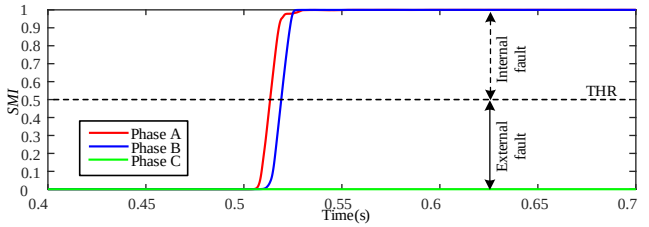

(c)

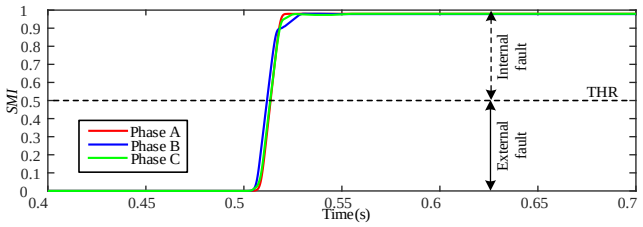

(d)

Fig. 19. Results for grey-highlighted part in Table I: (a) DCS, AG, 100 Ω; (b) DCS, AB, 0.1 Ω; (c) CS, ABG, 0.1 Ω; (d) CS, ABC, 50 Ω.

B. The Impact of Line Lengths and Fault Positions

To assess the impact of different line lengths and fault positions on the proposed protection across various operating states of BESS, fault positions are selected at 10 %, 50 %, and 90 % on line 19-33. The line lengths are 20 km, 60 km, and 100 km. All fault types are set to be AG, with fault resistance of 50 Ω. The results are tabulated in Table II, while the highlighted data are presented in Fig. 20.

From Table II and Fig. 20, it can be seen that the average operating time of the proposed protection is approximately 14 ms. Meanwhile, the minimum sensitivity of the protection can be clearly found as 1.94 for different fault positions and transmission line lengths. As a result, SMI-based protection can be adapted to different line lengths and still maintains high sensitivity and rapidity.

TABLE II. SIMULATION RESULTS AT DIFFERENT FAULT POSITIONS AND LINE LENGTHS.

Operating States	Line Length	Fault Position	*SMI*	Operating Time (ms)
Discharging state	20 km	10 %	1.0	11.8
		50 %	1.0	11.8
		90 %	1.0	12.0
	60 km	10 %	1.0	12.0
		50 %	1.0	12.0
		90 %	1.0	11.8
	100 km	10 %	1.0	12.0
		50 %	1.0	12.0
		90 %	1.0	12.0
Charging state	20 km	10 %	0.98	22.8
		50 %	0.98	15.0
		90 %	0.98	13.8
	60 km	10 %	0.97	23.2
		50 %	0.98	13.6
		90 %	0.98	13.8
	100 km	10 %	0.97	14.6
		50 %	0.98	13.8
		90 %	0.98	13.8

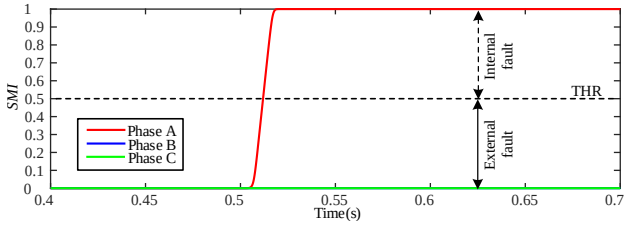

(a)

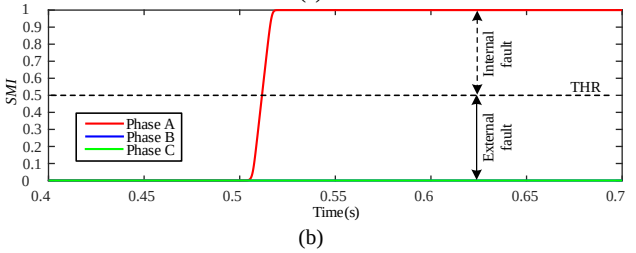

(b)

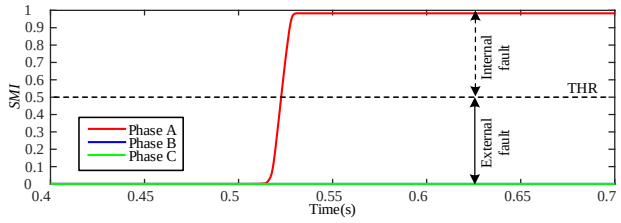

(c)

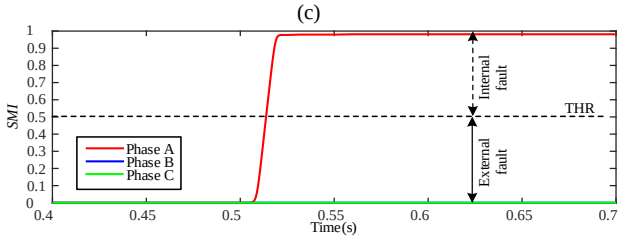

(d)

Fig. 20. Results for grey-highlighted part in Table II: (a) DCS, 60 km, 10 %; (b) DCS, 60 km, 90 %; (c) CS, 20 km, 10 %; (d) CS, 100 km, 90 %.

C. The Impact of Different Sampling Frequencies

When the protection method can adapt to different sampling frequencies, this means that it can better cope with different scenarios of realistic applications. Therefore, to study the impact of sampling frequencies on protection under different operating states of BESS, sampling frequency is selected as 2000 Hz, 4000 Hz, and 6000 Hz for simulation verification. The fault position is selected at 50 % of line 19-33from BESS, and the fault type is set as AG and AB. The results are tabulated in Table III, while the simulation waveforms corresponding to highlighted cases are presented in Fig. 21.

As can be seen from Table III and Fig. 21, when BESS operates in DCS, the proposed protection can operate correctly and maintain high sensitivity when faults occur at various sampling frequencies. When the BESS operates in CS, the sensitivity can still meet the requirements of line protection even in the case of 2000 Hz sampling frequency. Therefore, the proposed protection method can accommodate different sampling frequencies.

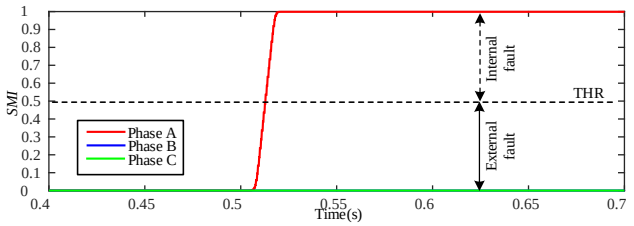

(a)

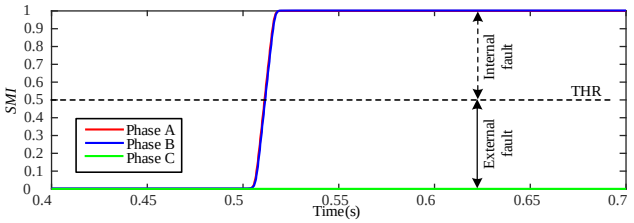

(b)

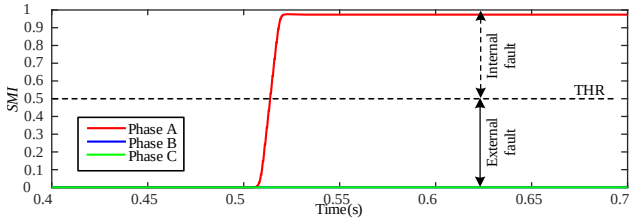

(c)

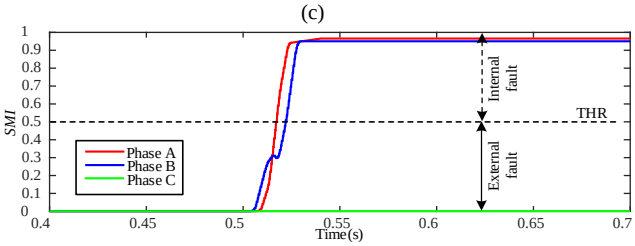

(d)

Fig. 21. Results for grey-highlighted part in Table III: (a) DCS, 2000 Hz, AG, 100 Ω; (b) DCS, 6000 Hz, AB, 50 Ω; (c) CS, 4000 Hz, AG, 100 Ω; (d) CS, 2000 Hz, AB, 50 Ω.

TABLE III. SIMULATION RESULTS AT DIFFERENT SAMPLING FREQUENCIES.

Operating States	Fault types	Fault Resistance	Sampling Frequency								
			2000 Hz			4000 Hz			6000 Hz		
			A	B	C	A	B	C	A	B	C
Discharging state	AG	0.1 Ω	1.0	0	0	1.0	0	0	1.0	0	0
		100 Ω	1.0	0	0	1.0	0	0	1.0	0	0
	AB	0.1 Ω	1.0	0.93	0	1.0	0.98	0	1.0	1.0	0
		50 Ω	1.0	1.0	0	1.0	1.0	0	1.0	1.0	0
Charging state	AG	0.1 Ω	1.0	0	0	1.0	0	0	0.99	0	0
		100 Ω	0.96	0	0	0.97	0	0	0.98	0	0
	AB	0.1 Ω	0.86	1.0	0	0.93	0.99	0	0.96	1.0	0
		50 Ω	0.95	0.95	0	0.96	0.96	0	0.98	0.98	0

D. The Robustness to Multiple Non-Ideal Conditions

External faults can sometimes occur with non-ideal conditions like CT error, CT saturation, and outliers, which may cause protection maloperation. Therefore, it is crucial to test the proposed protection security. The cases discussed below are all external faults occurring at bus 33. The BESS operates in CS, fault type is AG, and fault resistance is 0.1 Ω.

1. The Robustness to CT Saturation

To study the influence of CT saturation on the SMI-based protection, it is set that the grid-side CT is severely saturated. In this case, the current waveform and SMI are shown in Fig. 22.

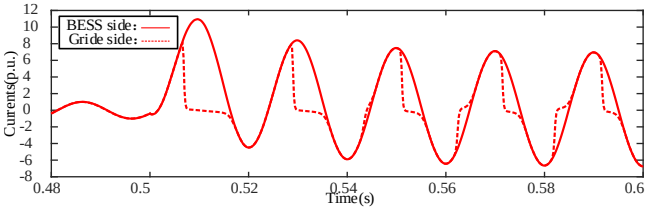

(a)

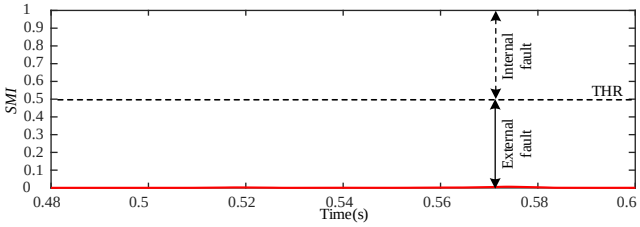

(b)

Fig. 22. Current waveforms and SMI under CT saturation: (a) Current waveforms; (b) SMI.

As can be seen from Fig. 22, when an external fault occurs and the CT is saturated, SMI is lower than THR; that is, SMI-based protection can ensure security without misoperation.

2. The Robustness to CT Error

So as to study the effect of CT error, the errors of the grid side's CT are set to −5 %, −10 %, +5 %, and +10 %, respectively. The current waveforms on both sides of lines 19-33 and SMI are shown in Fig. 23.

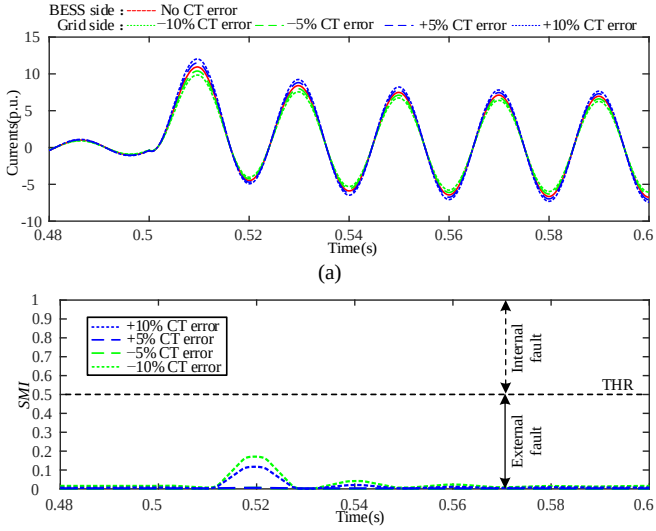

(a)

(b)

Fig. 23. Current waveforms and SMI under CT error: (a) Current waveforms; (b) SMI.

As shown in Fig. 23, SMI is still lower than THR even when the error of grid-side CT reaches ±10 %. That is, the security of the protection proposed in this study can be ensured in case of external faults with CT error.

3. The Robustness to Outliers

To study the influence of outliers, the currents on both sides are set to contain outliers. Current waveforms and SMI on both sides of line 19-33 are shown in Fig. 24.

Figure 24 illustrates significantly lower SMI values compared to THR during external faults with outliers. This confirms that the protection method introduced in this study can effectively handle outlier interference.

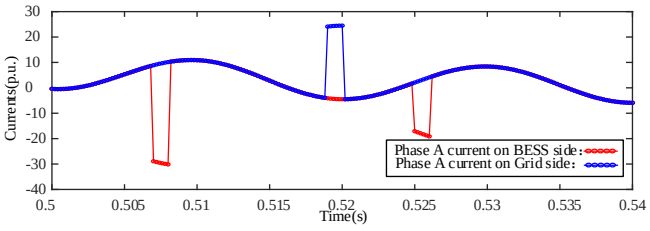

(a)

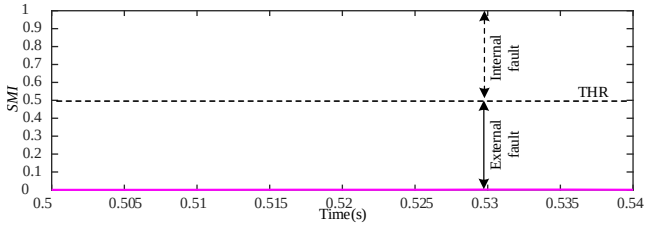

(b)

Fig. 24. Current waveforms and SMI in the presence of outliers: (a) Current waveforms; (b) SMI.

According to the results presented above, it can be clearly observed that the SMI-based protection provides dependability during internal faults and security during external faults, regardless of the operating states of BESS, with the added benefit of high sensitivity and rapidity.

V. DIGITAL-PHYSICAL CO-SIMULATION TESTING PLATFORM-BASED COMPARATIVE ASSESSMENT OF DIFFERENT PROTECTION METHODS

For further testing of SMI-based protection, a DPCS testing platform is constructed, as shown in Fig. 25 [30]. The experiments in this study primarily validate the correctness, sensitivity, and fault identification speed of the protection algorithm. The DPCS testing platform does not incorporate real-time delay factors external to the protection algorithm, such as communication and A/D conversion processes. Fiber-optic communication features high-speed transmission (1 ms/200 km) [18] and A/D conversion time is on the order of microseconds (μs). Thus, these delays have minimal impact. A 300 MW BESS is integrated with power grid through a 40 km line with parameters taken from [21], operating at a voltage level of 220 kV.

The performance of different protection methods is compared and then the advantages of SMI-based protection are highlighted. The compared protection methods include IED-based protection [11], FDI-based protection [12], and CTC-based protection [27]. The protection methods based on SMI and the three aforementioned protections are C-coded and run on digital signal processor (DSP) chip.

To facilitate the distinction, the three other protection methods are named method I, method II, and method III, in which the operating quantities are named IED, FDI, and CTC, respectively. Their thresholds IED_{thr}, FDI_{thr}, and CTC_{thr} are set to 0.3, 0.3, and 0.7, respectively.

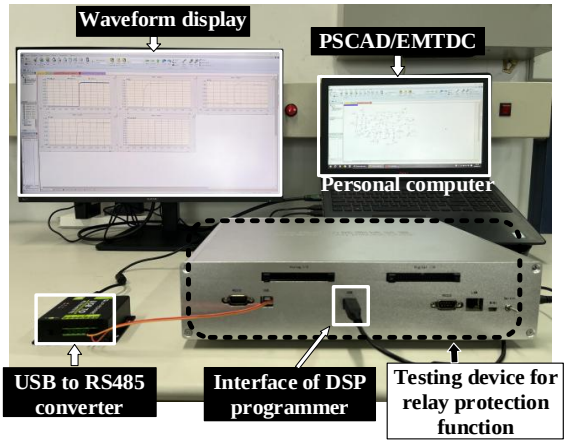

Fig. 25. Schematic diagram of DPCS testing platform.

A. *Dependability Comparison Test under Internal Faults*

Figure 26 shows the results of a comparative assessment of the dependability of the SMI-based protection and three protections under AG faults. These unbalanced faults were simulated 10 km from the BESS with varied fault resistances (20 Ω, 50 Ω, and 80 Ω).

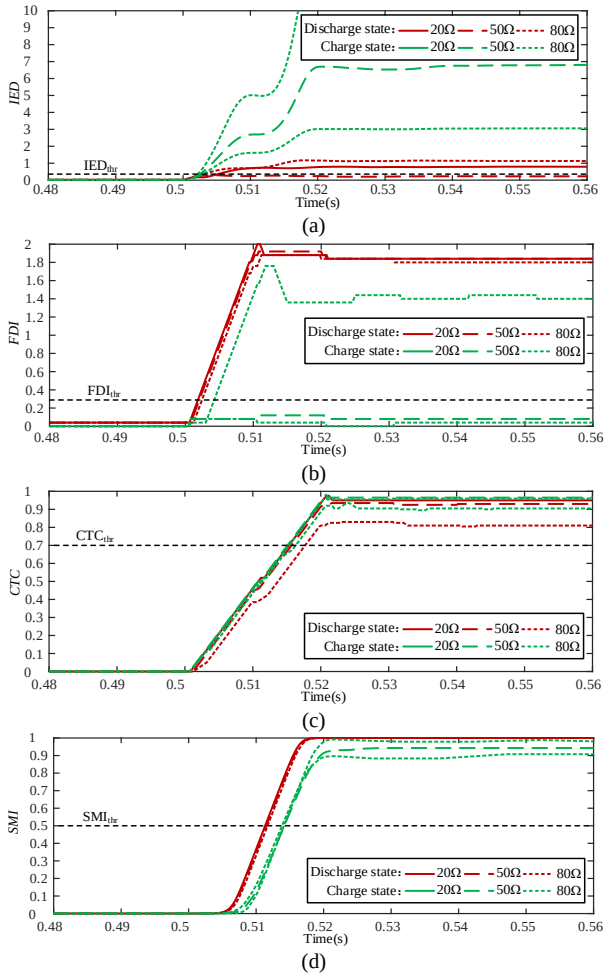

Fig. 26. Performance of four protection methods: (a) Method I; (b) Method II; (c) Method III; (d) SMI-based protection.

The conclusion from Fig. 26 is that method I is able to operate correctly when the BESS operates in CS. However, when BESS operates in DCS, method I cannot adapt to the change in fault resistances and will reject. On the contrary, protection II is able to operate correctly when BESS is in DCS, but cannot adapt to the change of fault resistances when BESS is in CS. In contrast, method III and SMI-based protection are able to adapt to different operating states and fault resistances of BESS. Nevertheless, the sensitivity of method III is lower compared to SMI-based protection. In conclusion, the SMI-based protection demonstrates greater dependability and sensitivity compared to the other three protection methods when internal faults occur.

B. *Comparative Evaluation of Robustness Against CT Saturation*

To assess the security of protection, an AG external fault (0.1 Ω) was simulated on the BESS-side bus with grid-side CT saturation, comparing the proposed SMI-based protection against three protections. The results of the experiment can be found in Fig. 27.

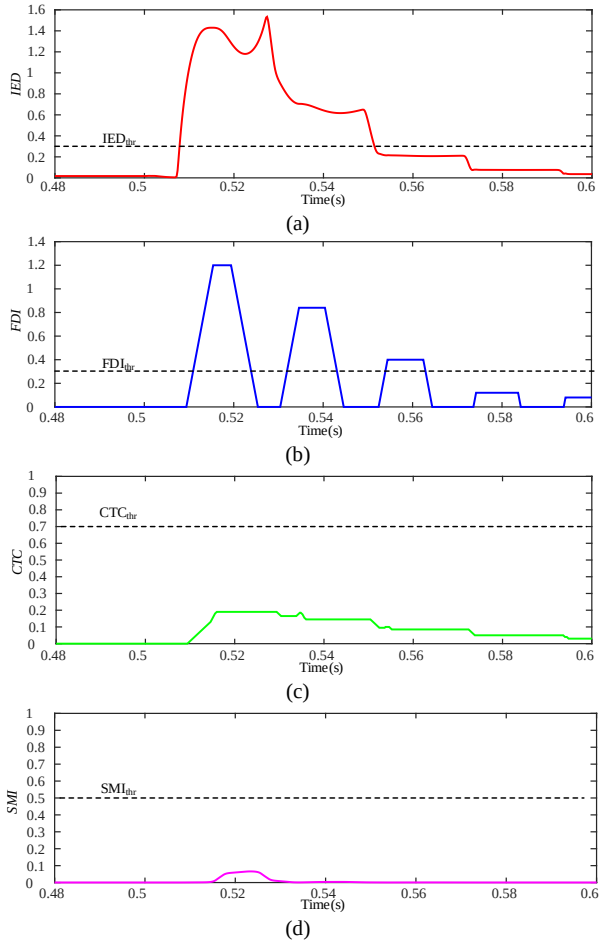

Fig. 27. Performance of four protection methods: (a) Method I; (b) Method II; (c) Method III; (d) SMI-based protection.

The CT saturation will cause distortion of the current waveform, resulting in reduced security of the protection method. From Fig. 27, both method I and method II are very sensitive to the waveform changes, resulting in misoperation and inability to ensure the security of the protection. As for method III and SMI-based protection, no misoperation occurs, which ensures the security of the SMI-based protection.

Comparative analysis demonstrates that SMI-based protection outperforms three existing methods for BESS-connected transmission lines, delivering superior dependability, security, sensitivity, and robustness.

VI. CONCLUSIONS

A pilot protection is proposed in this study to solve the issue related to the reduced adaptability of conventional relay protection in AC transmission lines connecting BESS.

With the innovative application of the character sequence matching index algorithm to relay protection, the SMI-based protection shows desirable performance in BESS-connected systems. In addition, the SMI-based protection is able to deliver superior response to different fault scenarios. The proposed protection scheme can usually identify faults within approximately one power frequency cycle, with the minimum sensitivity of protection in tests is greater than 1.5. For the sampling frequencies, SMI-based protection operates dependably at a wide range of sampling frequencies. The SMI-based protection's security is fully verified regarding disturbances including severe CT saturation, ±10 % error of CT, and outliers. Furthermore, the SMI-based protection is

compared with three recently proposed protections on digital-physical co-simulation platform. The experimental results show that the SMI-based protection is well adapted in AC transmission lines connecting BESS, as well as providing better security, dependability, and robustness.

CONFLICTS OF INTEREST

The authors declare that they have no conflicts of interest.

REFERENCES

[1] H. Holttinen *et al*., "Variable renewable energy integration: Status around the world", *IEEE Power and Energy Magazine*, vol. 19, no. 6, pp. 86–96, 2021. DOI: 10.1109/MPE.2021.3104156.

[2] C. Wang, X. Lin, J. Nan, J. Feng, W. Zhou, and H. Zhou, "Coordinating thermal energy storage capacity planning and multi-channels energy dispatch in wind-concentrating solar power energy system", *Journal of Cleaner Production*, vol. 350, art. 131405, 2022. DOI: 10.1016/j.jclepro.2022.131405.

[3] X. Zhao *et al*., "Low carbon scheduling method of electric power system considering energy-intensive load regulation of electrofused magnesium and wind powerfluctuation stabilization", *Applied Energy*, vol. 357, art. 122573, 2024. DOI: 10.1016/j.apenergy.2023.122573.

[4] Y. Yu, B. Wang, M. Li, and T. Lv, "Optimized distributed energy management for BESS incorporating time-varying delays with an improved bipartite grouping model simultaneously balancing SOH and SOC", *Journal of Energy Storage*, vol. 126, art. 117006, 2025. DOI: 10.1016/j.est.2025.117006.

[5] J. Li *et al*., "Dynamic economic evaluation of hundred megawatt-scale electrochemical energy storage for auxiliary peak shaving", *Protection and Control of Modern Power Systems*, vol. 8, no. 3, pp. 1–18, 2023. DOI: 10.1186/s41601-023-00324-8.

[6] M. Berger, I. Kocar, E. Farantatos, and A. Haddadi, "Modeling of Li-ion battery energy storage systems (BESSs) for grid fault analysis", *Electric Power Systems Research*, vol. 196, art. 107160, 2021. DOI: 10.1016/j.epsr.2021.107160.

[7] S. Chen, N. Tai, C. Fan, J. Liu, and S. Hong, "Sequence-component-based current differential protection for transmission lines connected with IIGs", *IET Generation, Transmission & Distribution*, vol. 12, no. 12, pp. 3086–3096, 2018. DOI: 10.1049/iet-gtd.2017.1507.

[8] H. Gao, J. Li, and B. Xu, "Principle and implementation of current differential protection in distribution networks with high penetration of DGs", *IEEE Transactions on Power Delivery*, vol. 32, no. 1, pp. 565–574, 2017. DOI: 10.1109/TPWRD.2016.2628777.

[9] L. Zang, G. Zou, C. Zhou, M. Zheng, and T. Du, "Ad-axis based current differential protection scheme for an active distribution network", *Protection and Control of Modern Power Systems*, vol. 7, no. 2, pp. 1–11, 2022. DOI: 10.1186/s41601-022-00243-0.

[10] Z. Liu, X. Yin, X. Yin, Q. Lu, J. Qiao, and Y. Wang, "A Dice similarity coefficient-based pilot protection method for 500kV transmission lines of large-scale integrated photovoltaic power supply", *Electric Power Systems Research*, vol. 226, art. 109918, 2024. DOI: 10.1016/j.epsr.2023.109918.

[11] Z. Yang, W. Liao, H. Wang, C. L. Bak, and Z. Chen, "Improved Euclidean distance based pilot protection for lines with renewable energy sources", *IEEE Transactions on Industrial Informatics*, vol. 18, no. 12, pp. 8551–8562, 2022. DOI: 10.1109/TII.2022.3148318.

[12] A. Saber, M. F. Shaaban, and H. H. Zeineldin, "A new differential protection algorithm for transmission lines connected to large-scale wind farms", *International Journal of Electrical Power & Energy Systems*, vol. 141, art. 108220, 2022. DOI: 10.1016/j.ijepes.2022.108220.

[13] A. Saber, H. H. Zeineldin, Tarek H. M. EL-Fouly, and A. Al-Durra, "A signed correlation index-based differential protection scheme for inverter-based islanded microgrids", *International Journal of Electrical Power & Energy Systems*, vol. 145, art. 108721, 2023. DOI: 10.1016/j.ijepes.2022.108721.

[14] X. Miao, D. Zhao, B. Lin, H. Jiang, and J. Chen, "A differential protection scheme based on improved DTW algorithm for distribution networks with highly-penetrated distributed generation", *IEEE Access*, vol. 11, pp. 40399–40411, 2023. DOI: 10.1109/ACCESS.2023.3269298.

[15] J. He, L. Xue, B. Li, Y. Li, E. Prieto-Araujo, and O. Gomis-Bellmunt, "Protection and fault ride-through techniques of VSC-HVDC systems for offshore wind power transmission—Research status, challenges, and prospects", *Renewable and Sustainable Energy Reviews*, vol. 210, art. 115138, 2025. DOI: 10.1016/j.rser.2024.115138.

[16] X. Li, L. Gui, J. Chen, and W. Jin, "Adaptive faulty phase selector for microgrids including battery energy storage stations", *Journal of Energy Storage*, vol. 90, part A, art. 111859, 2024. DOI: 10.1016/j.est.2024.111859.

[17] J. He *et al*., "Performance analysis and control-coordinated improvement method for distance protection of energy storage station grid-connected lines", *Applied Energy*, vol. 388, art. 125515, 2025. DOI: 10.1016/j.apenergy.2025.125515.

[18] Y. Liang, Y. Huo, and F. Zhao, "An accelerated distance protection of transmission lines emanating from MMC-HVdc stations", *IEEE Journal of Emerging and Selected Topics in Power Electronics*, vol. 9, no. 5, pp. 5558–5570, 2021. DOI: 10.1109/JESTPE.2021.3058154.

[19] J. Hou *et al*., "Improved differential protection for two-terminal weak feed AC system considering negative sequence control coordination strategy", *International Journal of Electrical Power & Energy Systems*, vol. 164, art. 110396, 2025. DOI: 10.1016/j.ijepes.2024.110396.

[20] Y. Zhang, Y. Yu, and G. Yang, "Adaptive current differential protection principle for transmission line connected to energy storage power station based on phase and amplitude compensation", *Journal of Energy Storage*, vol. 111, art. 115468, 2025. DOI: 10.1016/j.est.2025.115468.

[21] Y. Liang, Y. Ren, and W. He, "An enhanced current differential protection for AC transmission lines connecting MMC-HVDC stations", *IEEE Systems Journal*, vol. 17, no. 1, pp. 892–903, 2023. DOI: 10.1109/JSYST.2022.3155881.

[22] A. M. Joshua and K. P. Vittal, "Protection schemes for a battery energy storage system based microgrid", *Electric Power Systems Research*, vol. 204, art. 107701, 2022. DOI: 10.1016/j.epsr.2021.107701.

[23] A. M. Joshua and K. P. Vittal, "Superimposed current based differential protection scheme for AC microgrid feeders", *Applied energy*, vol. 341, art. 121079, 2023. DOI: 10.1016/j.apenergy.2023.121079.

[24] Z. Yang, R. Zhu, and W. Liao, "Minkowski distance based pilot protection for tie lines between offshore wind farms and MMC", *IEEE Transactions on Industrial Informatics*, vol. 20, no. 6, pp. 8441–8452, 2024. DOI: 10.1109/TII.2024.3369668.

[25] B. Zhou, B. Li, J. He, Y. Li, Z. Xie, and W. Dai, "A novel high-sensitivity time-domain current differential protection scheme for renewable power transmission system", *International Journal of Electrical Power & Energy Systems*, vol. 160, art. 110083, 2024. DOI: 10.1016/j.ijepes.2024.110083.

[26] W. Qin, Y. Cai, Q. Wei, X. Han, W. Chen, and Y. Jia, "Pilot protection scheme for transmission line of wind-storage combined system based on one-mode current similarity", *Electric Power Systems Research*, vol. 228, art. 110039, 2024. DOI: 10.1016/j.epsr.2023.110039.

[27] Y. Liang, C. Pan, and J. Zhang, "Current trajectory coefficient based time domain line protection for battery storage energy stations", *Journal of Energy Storage*, vol. 51, art. 104468, 2022. DOI: 10.1016/j.est.2022.104468.

[28] M. A. Jaro, "Advances in record-linkage methodology as applied to matching the 1985 census of Tampa, Florida", *Journal of the American Statistical Association*, vol. 84, no. 406, pp. 414–420, 1989. DOI: 10.1080/01621459.1989.10478785.

[29] *Instrument transformers — Part 2: Additional requirements for current transformers*, GB/T 20840.2-2014, Standards Press of China, China, Oct. 2014.

[30] J. R. Camarillo-Peñaranda, M. Aredes, and G. Ramos, "Hardware-in-the-loop testing of a distance protection relay", *IEEE Transactions on Industry Applications*, vol. 57, no. 3, pp. 2326–2331, 2021. DOI: 10.1109/TIA.2021.3066328.